nature geoscience

ARTICLES

https://doi.org/10.1038/s41561-018-0075-y

Lower-mantle plume beneath the Yellowstone hotspot revealed by core waves

Peter L. Nelson* and Stephen P. Grand

The Yellowstone hotspot, located in North America, is an intraplate source of magmatism the cause of which is hotly debated. Some argue that a deep mantle plume sourced at the base of the mantle supplies the heat beneath Yellowstone, whereas others claim shallower subduction or lithospheric-related processes can explain the anomalous magmatism. Here we present a shear wave tomography model for the deep mantle beneath the western United States that was made using the travel times of core waves recorded by the dense USArray seismic network. The model reveals a single narrow, cylindrically shaped slow anomaly, approximately 350 km in diameter that we interpret as a whole-mantle plume. The anomaly is tilted to the northeast and extends from the core–mantle boundary to the surficial position of the Yellowstone hotspot. The structure gradually decreases in strength from the deepest mantle towards the surface and if it is purely a thermal anomaly this implies an initial excess temperature of 650 to 850 °C. Our results strongly support a deep origin for the Yellowstone hotspot, and also provide evidence for the existence of thin thermal mantle plumes that are currently beyond the resolution of global tomography models.

Since the 1970s, some intraplate volcanoes have been hypothesized to originate from deep mantle plumes created by thermal instabilities along the core–mantle boundary (CMB)[1]. Classically, mantle plumes are viewed as warm mushroomed-shaped thermal anomalies that have a large spherical head with a long narrow vertical tail that is rooted at the CMB[2]. They have been postulated to be the cause of many prominent geologic features, such as large igneous provinces[3] and hotspot tracks, but their existence has not been universally accepted[4,5]. Determining the existence or nonexistence of deep thermal plumes is imperative to our understanding of mantle dynamics and interpretations of geochemically distinct reservoirs[6]. Recently, broad lower-mantle slow velocity conduits, most probably thermochemical in origin, have been associated with some hotspots, however, the direct detection of a classical thin plume in the lower mantle using travel time tomography has remained elusive[5,7,8].

The difficulty in detecting plumes in the lower mantle using seismic travel time tomography arises from the fact that they only weakly reduce the travel time (<0.5 s) of S waves (the primary phase used in most shear wave tomography models). This is because S wave ray paths in the deep mantle are largely subhorizontal whereas plumes are assumed to be subvertical, resulting in very little sampling of a deep plume by S waves (Fig. 1a). The small influence of plumes on S waves combined with wavefront healing effects makes imaging plumes difficult[9]. Furthermore, almost all hotspots with a purported deep-mantle origin are located in oceanic basins where seismic station coverage is poor[10]. One exception, however, is the Yellowstone hotspot, which is located in the interior of the western United States (Fig. 1b). The origin of the Yellowstone hotspot has been widely debated ever since the plume hypothesis was first proposed[11]. Evidence for a plume origin of the Yellowstone hotspot is provided by a 16.4-Myr-old volcanic track starting near the Columbia River Flood Basalts (CRB) that has followed plate movement[12], high He^3/He^4 ratios[13], a prominent regional geoid high[14] and a 12–18 km upward deflection of the 660 discontinuity[15]. Moreover, regional tomography studies have imaged a cylindrically shaped slow seismic anomaly extending from the hotspot to 900 km depth[15,16]. Below 900 km depth, these studies lose the resolution necessary to image the anomaly, if it is there. Despite evidence for a plume origin, Yellowstone has features not in accord with classical plume theory, such as a second hotspot track propagating in the opposite direction called the Newberry Trend, a 400 km gap between the western end of the main hotspot track and the largest eruption centres in the CRB, and the difficulty a plume would have in penetrating or bypassing nearby subducting slabs[17,18]. Alternative hypotheses for the hotspot attribute it to shallower lithospheric or subduction-related processes[17,19–21].

Seismic modelling and images

Here we present a new shear wave tomography model for the mantle beneath the western United States that is optimized to find short-wavelength, subvertical structures in the lower mantle. We find a structure that we interpret as a plume rising from the CMB that is probably the cause of the Yellowstone hotspot. We build on previous seismic tomography models by carefully analysing SKS and SKKS waves recorded by North American seismic stations (Fig. 1b). SKS phases travel as shear waves in the mantle and as compressional waves in the outer core. SKKS are similar to SKS, but they have one underside CMB reflection before they leave the core. The advantage of using SKS and SKKS is that their vertically oriented ray paths in the deep mantle (Fig. 1a) will traverse a potential plume for a greater distance than S, resulting in a larger travel time perturbation while still providing enough ray-crossing for accurate tomography. Additionally, the relative travel times of SKS and SKKS measured across a seismic array are insensitive to source side structure, as their ray paths are relatively close together there. Finally, the outer core should not affect variations in SKS and SKKS travel times due to its near homogeneous state[22]. Consequently, by effectively removing a mean travel time from each event, using SKS and SKKS wave travel time residuals we should be able to image short-wavelength, subvertical structures in the lower mantle beneath a dense array of seismic stations. Core waves alone, of course, are not sufficient to determine the complete three-dimensional (3D) variations in the mantle beneath the stations. Upper mantle anomalies, for example,

Department of Geological Sciences, Jackson School of Geosciences, The University of Texas at Austin, Austin, TX, USA. *e-mail: plnelson@utexas.edu

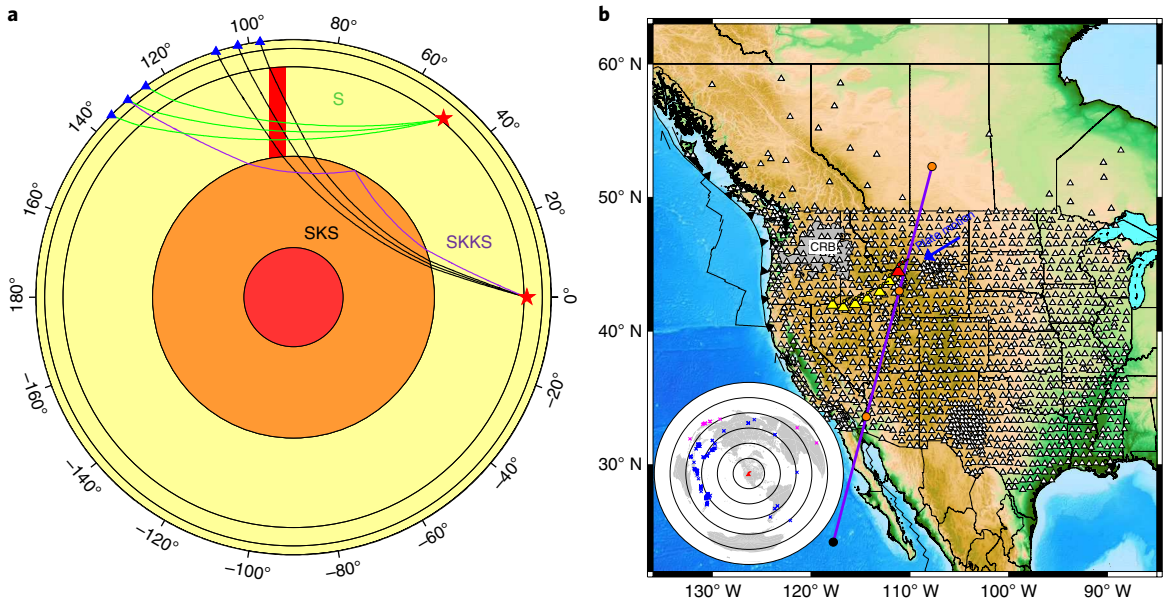

Fig. 1 | Diagram of S, SKS and SKKS ray paths and a map of station and event locations with geologic features of the Yellowstone hotspot. a, Comparison of S, SKS and SKKS ray paths through a simple plume structure (red rectangle) from 600-km-deep sources (red stars) to stations (blue triangles). Thin black lines show the 410 and 660 km discontinuities. Note the differences in the orientation and distance of SKS ray paths through the plume structure compared with S ray paths in the lower mantle and the closeness of the SKS ray paths on the source side. **b**, Map of the Yellowstone hotspot and surrounding region. White triangles indicate the locations of the seismometers used in our experiment. The red volcano is the current location of the Yellowstone hotspot. The CRB is located at the end of the hotspot track (yellow volcanos), which has followed plate motion. The purple line is the location of the cross-section shown in Fig. 3. Inset: Map of the events we measured SKS (blue crosses) and SKKS (magenta crosses) travel times from, respectively. Contour lines are in 30° increments away from Yellowstone (red volcano).

cannot be resolved well by such waves because their ray paths become too close to vertical to cross there.

The data set we use consists of over 26,000 SKS and SKKS travel time residuals from 71 events (Fig. 1b) measured in two frequency bands (2–10 s and 10–100 s) using a modified version of the adaptive stacking technique (see Methods). We applied corrections for crustal structure, station elevation and ellipticity to the travel times. Additionally, the travel times were corrected for radial anisotropy, as discussed more fully in the Methods. We calculated travel time sensitivity kernels using the finite frequency theory developed by a previous study[23]. We included up to the third Fresnel zone in the kernels based on comparisons with exact calculations using the spectral-element method[24]. Travel time residuals were then determined using the finite frequency kernels with respect to several global shear wave tomography models including S40RTS[25], SEMUCB-WM1[26], TX2016[27] and the regional model US-SL-2014[28]. We also used an average of the global models for the lower mantle smoothed into US-SL-2014 to compute a set of residuals. For each earthquake, an appropriate source term was removed (See Methods). Finally, we inverted the residuals using the LSQR algorithm[29] regularized by second-order Laplacian smoothing and damping constraints.

Figures 2 and 3 show our results; for which we used the average of the seismic models, discussed above, as the starting model in the inversion. In Supplementary Figs. 1–5, we show results using each individual model as the starting model. The most striking feature in the lower mantle of our inverted model is a ~350-km-diameter cylindrical-shaped slow anomaly that is continuous from the CMB to the surface near Yellowstone. It is rooted at the CMB near the Mexico/California border (Fig. 2) and has an overall tilt to the northeast with a strong offset from 900–1,300 km depth. The amplitude of the anomaly also changes with depth. In the deepest mantle the anomaly has a peak near 2% decreasing steadily to about 1% at 1,000 km depth. Larger-amplitude anomalies exist in the upper mantle. The overall profile and amplitude of the anomaly is generally consistent regardless of what starting model we use (Supplementary Figs. 1–5). We do not observe any other significant continuous fast or slow structures in the lower mantle. With regard to fast anomalies, our results are consistent with earlier studies, which have shown that the Farallon slab is mainly to the east of our study region[30]. Comparisons with the global tomography starting models at the CMB show that they all have regions that are notably slower than their surroundings in the proximity of where our anomaly is rooted. However, they do not have the resolution to image structures at the wavelengths of the anomaly we show here.

Resolution tests

To assess the reliability of our results, we conducted linear resolution tests in which we created a data set using synthetic plumes and checked whether we could recover the structures (see Methods). The synthetic plumes we used are 250 km in diameter with a Gaussian velocity distribution with a peak of 2%. Travel time residuals were calculated using finite frequency kernels with 0.5 s of random noise added. The tests (Fig. 4) indicate the feature we imaged under Yellowstone is laterally well resolved and is unlikely to be caused by vertical smearing. This test also shows that our model most likely underpredicts the true amplitude of anomalies by 25–40%. We also performed additional tests to examine our ability to resolve a tilted plume structure similar to the one we imaged (Supplementary Figs. 7 and 8). The results show that in the lower mantle we are able to resolve the structure well, however above 1,300 km the increase in tilt and near-vertical orientation of the SKS and SKKS ray paths cause a notable drop in the recovered amplitude (see Methods).

Plume characteristics and comparison with geodynamic predictions

The anomaly's proximity to the Yellowstone hotspot, continuity across the whole mantle and cylindrical morphology are consistent with it being a thermal plume. Assuming the derivative of

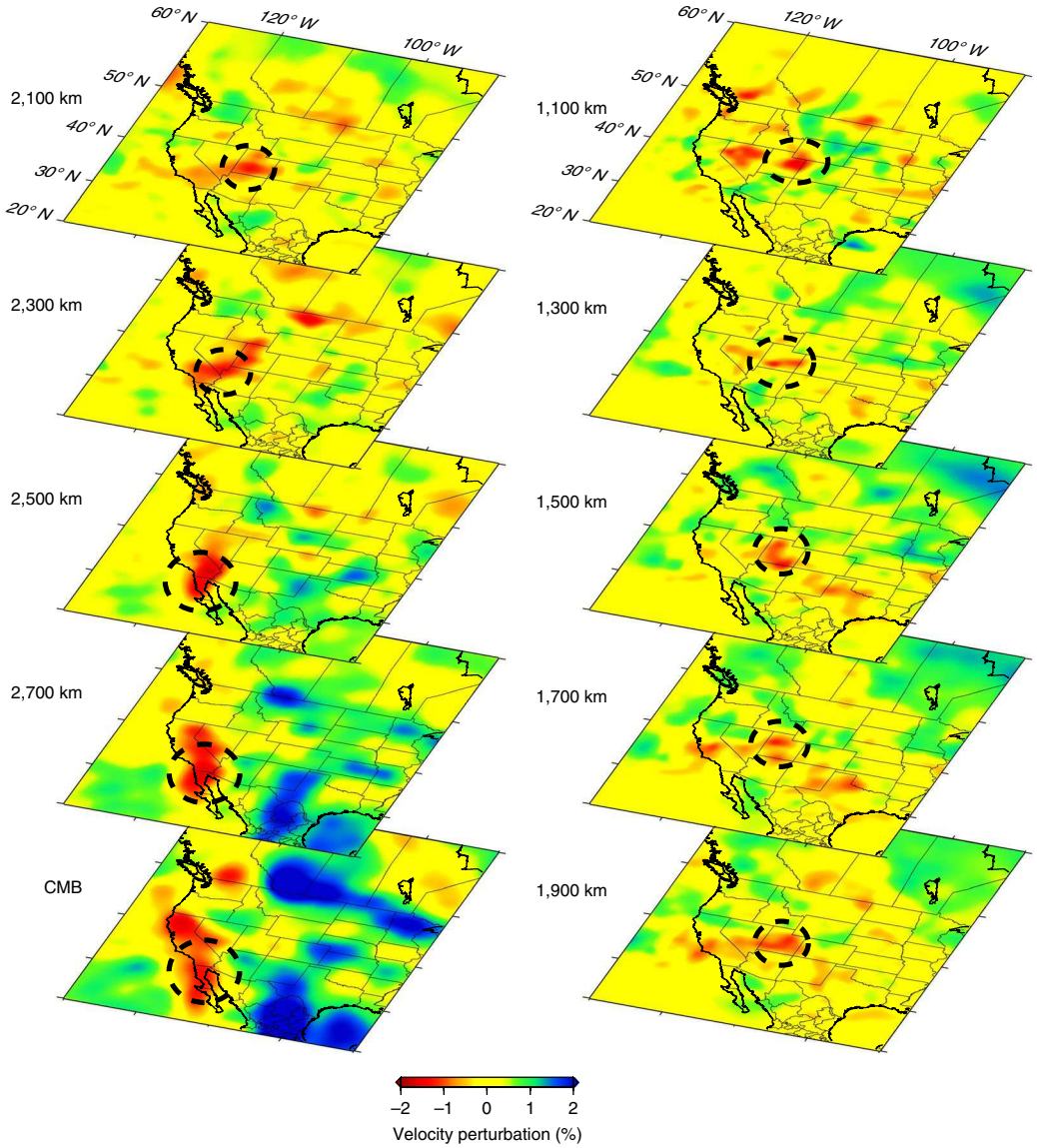

Fig. 2 | Tomographic images of the lower mantle. Slow anomalies are shown in red while fast anomalies are shown in blue, with depth indicated to the left of each slice. Note that the same colour scale is used for all depth slices. The dashed circles show the location of the structure that we interpret as a plume; it is the slowest feature in each slice and is continuous from the CMB to the surface.

shear velocity with respect to temperature is 0.4% per 100 °C[31], the peak excess temperature within the plume is 650–850 °C in the deepest mantle, decreasing to nearly half of that value at the top of the lower mantle. Here we assumed that our seismic model has an amplitude 25–40% less than the true structure, which is probably a minimum estimate because of possible errors not included in the resolution analysis (see Methods). The deep excess temperature, as well as its decrease towards the surface, are consistent with geodynamic simulations of thermal plumes[32,33]. Additionally, the anomaly we imaged is not vertical but is tilted to the northeast. A previous study[34] showed that upwelling mantle plumes should be tilted as they ascend due to mantle-wide convection (mantle wind). In those simulations, a potential plume feeding Yellowstone would indeed be tilted to the northeast, although it should be noted that the tilt we found is larger than his prediction, suggesting a stronger influence of lower-mantle wind on the plume. The discrepancy could indicate stronger convective flow in the deepest mantle and the top of the lower mantle or a slower ascent velocity of the plume relative to the model used in earlier work[14]. We also find that the plume ascent is most strongly shifted laterally between 900 and 1,300 km depth. Other studies have noted unusual behaviour at this depth, both for upwelling regions and subducted slabs[7,35], perhaps due to a rapid change in viscosity near these depths[36].

We conclude that a plume rising from the CMB is the ultimate heat source driving Yellowstone volcanism. Fig. 3 shows that there is a large volume of upper mantle with slow velocity to the south of Yellowstone beneath the Basin and Range province. This low-velocity feature is unlikely to be related to the lower-mantle plume that we have imaged. The anomaly only starts to appear near 700 km depth and becomes widespread throughout the southwestern United States in the transition zone, whereas the structure in the lower mantle seems to focus beneath Yellowstone (Supplementary Fig. 6). Furthermore, none of our inversions show any direct connection at depth between the two features (Supplementary Fig. 5). Finally, as mentioned previously, there is a prominent geoid high at Yellowstone relative to the rest of the western United States[14] along with exclusively high He^3/He^4 ratios found in the basalts erupted there[13]. These observations suggest that the heat source beneath

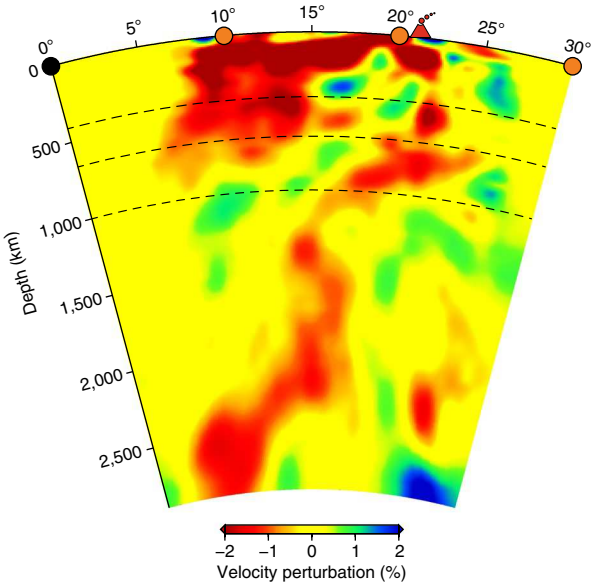

Fig. 3 | Depth cross-section through the plume structure showing its connection with the Yellowstone hotspot. The location of the cross-section is shown by the purple line in Fig. 1, with black and orange circles indicating positions along the cross-section. The surficial position of the Yellowstone hotspot is shown by the red volcano. Dashed lines indicate 410, 660 and 1,000 km depth. The colour bar was chosen to highlight lower-mantle features. Anomalies in the upper mantle mainly reflect the choice of starting model (US-SL-2014)[28].

Yellowstone is unique relative to the rest of the western United States. The broad, slow region in the upper mantle is more probably related to shallow tectonic processes such as extension in the Basin and Range, delamination of lithosphere or mantle hydration caused by the subducting slab[37], rather than originating from the narrow lower-mantle structure we imaged.

Recent tomography studies[7,8] have found large subvertical slow seismic anomalies in the lower mantle that are associated with surface hotspots. These 'plumes' are volumetrically larger and probably slower than the Yellowstone plume imaged here. They are also associated with large low-shear-velocity provinces (LLSVPs)[10] at the base of the mantle whereas Yellowstone is located far from LLSVPs. Geodynamic simulations investigating plumes originating from thermochemical boundary layers have found that the evolution of plumes is strongly controlled by the thickness and strength of the thermal and chemical basal layers[32]. In particular, plumes originating from thick thermochemical boundaries will be hotter and volumetrically larger than purely thermal plumes. The basal layers of the LLSVPs could be hotter and intrinsically denser than where Yellowstone originates, providing a different set of boundary conditions that govern plume growth. Why Yellowstone originates where it does is still unclear, however, it has been suggested that the low-velocity region where the Yellowstone plume is rooted was once a small piece of the Pacific LLSVP that has been sheared off by a subducting slab[38]. It could also be a purely thermal plume generated at the thermal boundary layer at the CMB. Regardless of the cause, our results strongly support a deep-mantle plume origin for the Yellowstone hotspot and the CRB as opposed to a shallower origin[17,19–21]. Plumes such as the one imaged here would not be resolved by global tomography and thus could exist elsewhere.

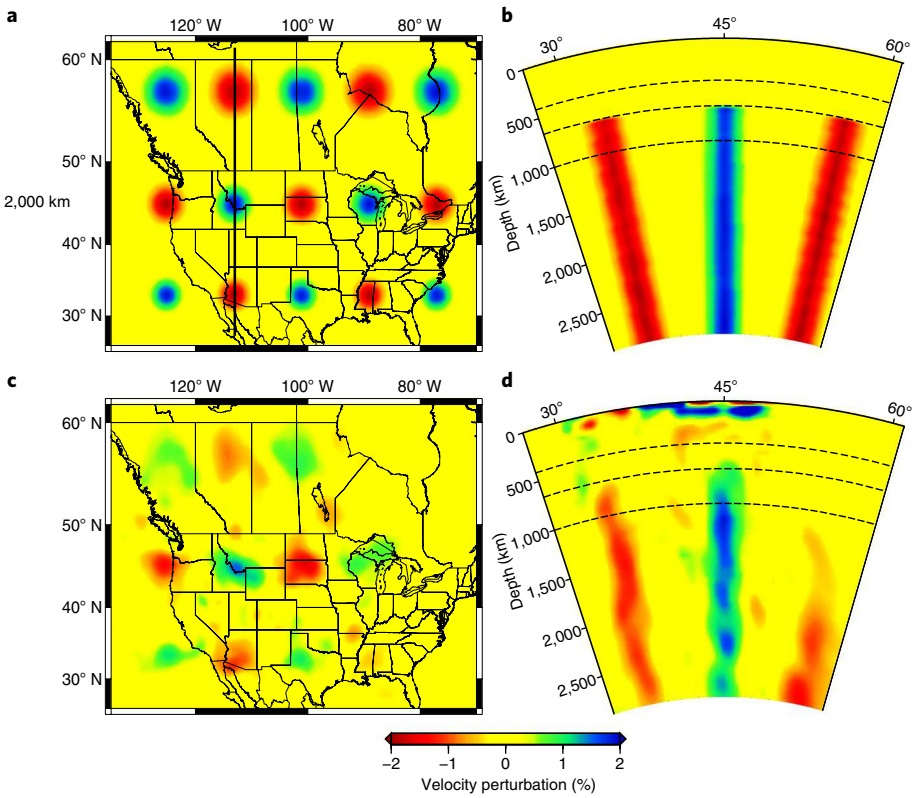

Fig. 4 | Resolution test results for 250-km-diameter plume structures. a, Starting model, which has a number of 250-km-diameter lower-mantle plume structures with a maximum amplitude of 2%. **b**, Corresponding cross-section along the black line in **a**. **c**, Recovered structures after inversion with a random distribution of 0.5 s added to the synthetic data. **d**, Corresponding cross-section along the black line in **a**. The test shows good recovery in the interior of the western United States, but much poorer recovery where the station coverage is less dense (Fig. 1).

Methods

Methods, including statements of data availability and any associated accession codes and references, are available at https://doi.org/10.1038/s41561-018-0075-y.

Received: 27 September 2017; Accepted: 1 February 2018;
Published online: 19 March 2018

References

1. Morgan, W. J. Convection plumes in the lower mantle. *Nature* **230**, 42–43 (1971).
2. Campbell, I. H. Testing the plume theory. *Chem. Geol.* **241**, 153–176 (2007).
3. Coffin, M. F. & Eldholm, O. Large igneous provinces: crustal structure, dimensions, and external consequences. *Rev. Geophys.* **32**, 1–36 (1994).
4. Foulger, G. R. *Plates vs Plumes: A Geological Controversy* (Wiley-Blackwell, Hoboken, 2011).
5. Anderson, D. L. & Natland, J. H. Mantle updrafts and mechanisms of oceanic volcanism. *Proc. Natl Acad. Sci. USA* **111**, E4298–E4304 (2014).
6. Hofmann, A. W. Mantle geochemistry: the message from oceanic volcanism. *Nature* **385**, 219–229 (1997).
7. French, S. W. & Romanowicz, B. Broad plumes rooted at the base of the Earth's mantle beneath major hotspots. *Nature* **525**, 95–99 (2015).
8. Montelli, R., Nolet, G., Dahlen, F. A. & Masters, G. A catalogue of deep mantle plumes: new results from finite-frequency tomography. *Geochem. Geophys. Geosyst.* **7**, Q11007 (2006).
9. Maguire, R., Ritsema, J., van Keken, P. E., Fichtner, A. & Goes, S. *P*- and *S*-wave delays caused by thermal plumes. *Geophys. J. Int.* **206**, 1169–1178 (2016).
10. Courtillot, V., Davaille, A., Besse, J. & Stock, J. Three distinct types of hotspots in the Earth's mantle. *Earth Planet. Sci. Lett.* **205**, 295–308 (2003).
11. Fouch, M. J. The Yellowstone hotspot: plume or not? *Geology* **40**, 479–480 (2012).
12. Smith, R. B. & Braile, L. W. The Yellowstone hotspot. *J. Volcanol. Geotherm. Res.* **61**, 121–129 (1994).
13. Graham, D. et al. Mantle source provinces beneath the northwestern USA delimited by helium isotopes in young basalts. *J. Volcanol. Geotherm. Res.* **188**, 128–140 (2009).
14. Smith, R. B. et al. Geodynamics of the Yellowstone hotspot and mantle plume: Seismic and GPS imaging, kinematics, and mantle flow. *J. Volcanol. Geotherm. Res.* **188**, 26–56 (2009).
15. Schmandt, B., Dueker, K., Humphreys, E. & Hansen, S. Hot mantle upwelling across the 660 beneath Yellowstone. *Earth Planet. Sci. Lett.* **331**, 224–236 (2012).
16. Obrebski, M., Allen, R. M., Xue, M. & Hung, S. H. Slab-plume interaction beneath the Pacific Northwest. *Geophys. Res. Lett.* **37**, L14305 (2010).
17. Foulger, G. R, Christiansen, R. L. & Anderson, D. L. *The Yellowstone "Hot Spot" Track Results from Migrating Basin-range Extension*. Geological Society of America Special Papers 215–238 (2015).
18. Leonard, T. & Liu, L. The role of a mantle plume in the formation of Yellowstone volcanism. *Geophys. Res. Lett.* **43**, 1132–1139 (2016).
19. James, D. E., Fouch, M. J., Carlson, R. W. & Roth, J. B. Slab fragmentation, edge flow and the origin of the Yellowstone hotspot track. *Earth Planet. Sci. Lett.* **311**, 124–135 (2011).
20. Long, M. D. Mantle dynamics beneath the Pacific Northwest and the generation of voluminous back-arc volcanism. *Geochem. Geophys. Geosyst.* **13**, Q0AN01 (2012).
21. Liu, L. & Stegman, D. R. Origin of Columbia River flood basalt controlled by propagating rupture of the Farallon slab. *Nature* **482**, 386–389 (2012).
22. Stevenson, D. J. Limits on lateral density and velocity variations in the Earth's outer core. *Geophys. J. Int.* **88**, 311–319 (1987).
23. Dahlen, F., Hung, S.-H. & Nolet, G. Fréchet kernels for finite-frequency traveltimes—I. Theory. *Geophys. J. Int.* **141**, 157–174 (2000).
24. Tromp, J., Komattisch, D. & Liu, Q. Spectral-element and adjoint methods in seismology. *Commun. Comput. Phys.* **3**, 1–32 (2008).
25. Ritsema, J., Deuss, A., Van Heijst, H. & Woodhouse, J. S40RTS: a degree-40 shear-velocity model for the mantle from new Rayleigh wave dispersion, teleseismic traveltime and normal-mode splitting function measurements. *Geophys. J. Int.* **184**, 1223–1236 (2011).
26. French, S. W. & Romanowicz, B. A. Whole-mantle radially anisotropic shear velocity structure from spectral-element waveform tomography. *Geophys. J. Int.* **199**, 1303–1327 (2014).
27. Lu, C. & Grand, S. P. The effect of subducting slabs in global shear wave tomography. *Geophys. J. Int.* **205**, 1074–1085 (2016).
28. Schmandt, B. & Lin, F. C. P and S wave tomography of the mantle beneath the United States. *Geophys. Res. Lett.* **41**, 6342–6349 (2014).
29. Paige, C. C. & Saunders, M. A. Towards a generalized singular value decomposition. *SIAM J. Numer. Anal.* **18**, 398–405 (1981).
30. Sigloch, K. Mantle provinces under North America from multifrequency P wave tomography. *Geochem. Geophys. Geosyst.* **12**, Q02W08 (2011).
31. Stixrude, L. & Lithgow-Bertelloni, C. Geophysics of chemical heterogeneity in the mantle. *Annu. Rev. Earth Planet. Sci.* **40**, 569–595 (2012).
32. Lin, S. C. & van Keken, P. E. Dynamics of thermochemical plumes: 1. Plume formation and entrainment of a dense layer. *Geochem. Geophy. Geosyst.* **7**, c001071 (2006).
33. Leng, W. & Zhong, S. Controls on plume heat flux and plume excess temperature. *J. Geophys. Res. Solid Earth* **113**, B04408 (2008).
34. Steinberger, B. Plumes in a convecting mantle: models and observations for individual hotspots. *J. Geophys. Res. Solid Earth* **105**, 11127–11152 (2000).
35. Fukao, Y. & Obayashi, M. Subducted slabs stagnant above, penetrating through, and trapped below the 660 km discontinuity. *J. Geophys. Res. Solid Earth* **118**, 5920–5938 (2013).
36. Rudolph, M. L., Lekić, V. & Lithgow-Bertelloni, C. Viscosity jump in Earth's mid-mantle. *Science* **350**, 1349–1352 (2015).
37. Schmandt, B. & Humphreys, E. Complex subduction and small-scale convection revealed by body-wave tomography of the western United States upper mantle. *Earth Planet. Sci. Lett.* **297**, 435–445 (2010).
38. Steinberger, B. M. Geodynamic models of a Yellowstone plume and its interaction with subduction and large-scale mantle circulation. In *AGU Fall Meeting* abstr. V11E-05 (Americal Geophysical Union, 2012).

Acknowledgements

We like to thank K. Tao and F. Zhang for helpful discussions about finite frequency tomography and S.-H. Hung for providing the tomography code. We also thank S. Yu and E. Garnero for providing the adaptive stacking travel time measurement code and B. Steinberger for useful discussion. Lastly, we thank P. Crotwell for help with S.O.D (Standing Order for Data) and the IRIS (Incorporated Research Institution for Seismology) Data Center and the Canadian National Data Center for providing the waveforms used in this experiment. This work was supported by the National Science Foundation grant EAR 1648770.

Author contributions

S.P.G. designed the project. P.L.N. undertook the data measurements and tomography. P.L.N. and S.P.G cowrote the manuscript.

Competing interests

The authors declare no competing interests

Additional information

Supplementary information is available for this paper at https://doi.org/10.1038/s41561-018-0075-y.

Reprints and permissions information is available at www.nature.com/reprints.

Correspondence and requests for materials should be addressed to P.L.N.

Publisher's note: Springer Nature remains neutral with regard to jurisdictional claims in published maps and institutional affiliations.

Methods

Data and travel time measurements. In total, our data set consisted of 25,428 SKS (40% 2–10 s, 60% 10–100 s) and 1,352 SKKS (100% 10–100 s) travel times measured in two separate frequency bands on the radial component of displacement seismograms. We used magnitude 5.6 or greater events that were at distances between 85°–130° for SKS and distances greater than 130° for SKKS to ensure minimum interference with other major arrivals. For SKS at distances less than 108° and all SKKS, we measured relative travel times using a modified version of the adaptive stacking technique[39]. First, we preprocessed the seismograms by removing the mean, trend and instrument response. Next, we bandpass-filtered the data into the desired frequency range using a two-pole two-pass Butterworth filter. After preprocessing, we aligned the traces using PREM's[40] predicted arrival times for SKS/SKKS and selected a window, usually between 20–30 s long, around the arrival times. We then stacked the selected segments to form an average wavelet, which we cross-correlated with each trace to determine a cross-correlation coefficient (CCC) and a best correlation time shift. We applied the time shifts to improve the alignment between the traces and then restacked them to reform the average wavelet. Additionally, we used the CCC and the signal to noise (SNR) of each trace as weights when updating the wavelet. The SNR was determined by comparing the amplitude of the SKS/SKKS arrival to the average amplitude of a section of the seismogram where we did not expect any arrivals. Traces with SNR or CCC below a threshold were omitted from the updated average wavelet. The process was repeated until the average wavelet converged, usually less than five iterations. The relative travel times we used in our inversions only included data that made it into the final stacks. Lastly, each measurement was visually inspected to ensure a good fit and if necessary, slightly adjusted (<0.25 s) or removed from the data set.

SKpdiffS measurements. For events with stations greater than 108°away, there is a second arrival called SKpdiffS that greatly distorts the backend of the SKS waveforms. SKpdiffS occurs when an SKS is incident to the CMB at the critical angle for ScP, an S wave that is reflected as a P wave at the CMB. The phase is commonly used to study the lowermost mantle because its onset and amplitude is highly sensitive to the structure there[41]. To account for this phase, we first created an average wavelet following the procedure described above only using stations <108°, which are unaffected by SKpdiffS. Next, we calculated approximate Green's functions for PREM using the reflectivity method[42] and convolved those with the average wavelet for each event to make synthetic seismograms. We included no upgoing waves or attenuation in our reflectivity calculations so that they represent an impulse at shorter distances. To see if our synthetic seismograms fit the observed SKpdiffS behaviour, we compared the data and synthetic seismograms stacked into 1° distance bins and checked if the timing and relative amplitude between the two phases was correct. If the SKpdiffS was poorly fit by PREM, we found, by trial and error, the best fitting model we could by reducing both the S and P velocity in a 3:1 ratio at the bottom 20 km of the mantle[41]. Afterwards, we cross-correlate the synthetic seismograms made using the best model for SKpdiffS with all of the recorded data. As before, we manually inspect each measurement and if necessary slightly adjust or remove them.

Traveltime corrections. We applied a series of small corrections to our travel times to mitigate the effects of some necessary simplifications we imposed on our model. We treated measurements made in each frequency band separately. First, we made standard ray theory-based crustal, topography and ellipticity corrections[43] using the upper, middle and lower crust layers of CRUST 1.0[44] and AK-135 ellipticity coefficients[45]. Although SKS and SKKS source side mantle ray paths are very close, they can accumulate non-negligible travel time differences if they travel through areas with high velocity gradients. To better account for this, we computed source-only side finite frequency kernels on a $1°\times1°$ grid and remove their predicted travel time residuals using three global models, S40RTS[25], SEMUCB-WM1[26] and TX2016[27]. We also used an average model, computed as the arithmetic mean of the three global models. The relative time differences between stations on the source side were usually small (<0.25 s), however, for events with source-side ray paths near an edge of a large low shear-velocity province the differences were more significant.

Additionally, we account for the effects of radial anisotropy in the upper mantle by applying a first-order correction to our travel times. Assuming the medium is radially anisotropic, the radial component $R(t)$ of a seismogram can be written in terms of the fast- and slow-polarized waves as

$$R(t) = s(t)\cos^2\phi + s(t-\delta t)\sin^2\phi$$

where $s(t)$ is the signal in an isotropic earth, ϕ is the polarization angle and δt is the delay time[46]. It can be shown to first order using Taylor expansions that

$$t_{\text{isotropic}} = t_{\text{measured}} - \delta t \sin^2\phi$$

We used SKS splitting parameters from ref.[47] for stations located in the United States, while for Canadian stations we used parameters from refs [48–51]. For stations without available splitting measurements, we used the nearest station's parameters as a substitute. If there were no nearby stations then we treated the station as isotropic. Final residuals were calculated relative to several published seismic models using finite frequency kernels. We used an averaged model consisting of the regional model US-SL-2014[28] above 1,000 km depth for the mantle beneath the United States and an average of the global models for the mantle below. Because the models do not exactly agree at 1,000 km, we smoothed them together by using a weighted sum between 1,000 km and 1,200 km depth.

Due to the fact that the USArray migrated across the United States, each earthquake had a different set of stations for which travel time measurements were made. Thus, it was inappropriate to take out a mean of residuals for each event as is commonly done in regional tomography studies. Following the procedure of a previous study[52], we inverted for event and station statics with the constraint that the average station static was 0. We note that the statics are with respect to predictions of the 3D starting model. We also applied weights to the inversion by first separating our events into 5° azimuthal bins. We then determined the weight for each event by dividing the average number of events per bin by the number of events in that event's particular bin. The event static is an effective mean for each event whereas the station static is mainly the signal from the crust and uppermost mantle underneath a particular station that is unaccounted for in the starting model. We removed both the event and station statics from the data to get a set of travel time residuals. Using this data set, we calculated new earthquake locations and origin times constrained to be within a $50\times50\times50$ km^3 box around the original location[53]. Our new earthquake locations are unlikely to be the true hypocentre due to the limited azimuthal range and the single phase we use. However, this is an effective way of removing long wavelength variations in the data caused by a near-source structure, as well as earthquake mislocation. After adjusting the original travel times for the new locations, we reapplied all of our previous corrections and recalculated event and station statics.

Parameterization and inversion. We parameterized our model space (21° N to 63° N and 80° W to 140° W on the surface) into evenly spaced 50 km grid points from the surface down to the CMB. To invert our travel times for mantle velocity perturbations, we calculated finite frequency kernels up to the third Fresnel zone using the paraxial approximation as described by an earlier work[23]. We used the spectrums of the average wavelets we constructed for travel time measurements as the source term in the kernel calculations. To test the accuracy of our kernels, we compared their travel times predictions for a simple synthetic lower-mantle plume structure against the travel times of synthetics made with SPECFEM3D[24] and found them in good agreement.

We solved the system of equations relating travel time residual to velocity perturbation using an iterative LSQR[29] algorithm regularized by second-order Laplacian smoothing and damping constraints. The regularization parameters were chosen based on the L-curve criteria[54]. In addition to our regularization constraints, we also applied the same azimuthal weights that we used to calculate the event and station statics to the inversion. To mitigate contamination caused by unaccounted crust and uppermost mantle structure on our lower mantle, we applied a two-phase inversion technique in which we first inverted for only the top 100 km of our model before we allowed deeper variations.

Data uncertainty and resolution tests. An important issue is whether our travel time measurements are accurate enough to resolve a potential plume structure in the lower mantle. To estimate the uncertainty of our measurements, we compared residuals between two nearby deep events (200710050717 and 200710162105) after all the corrections were applied. The standard deviation between common stations for both frequency bands is <0.25 s while the delay we expect from a plume on SKS and SKKS is on the order of ~1–2 s. Errors caused by the differences in location and frequency content of the source are included in this estimate, which could account for some of the disagreement between the measurements.

As discussed in the main text, we performed linear resolution tests to determine how reliable our results are. We did this by first creating a model with synthetic lower mantle plume structures that were 250 km in diameter with a 2% Gaussian velocity distribution alternating between fast and slow (Fig. 4a). We then used the same station–event pairs as our data to calculate residuals with respect to the synthetic model using our finite frequency kernels. Furthermore, we added a random distribution of noise with a standard deviation of 0.5 s to the synthetic data. Finally, we inverted the data using the same regularization parameters and two-phase method as for our real data. The results of the test (Fig. 4b) show in the contiguous United States, where we imaged the plume, we see no indication of substantial smearing or gaps in recovery, however the amplitude is reduced by 25–40% in the cores of the plumes.

To assess our ability to resolve a tilted structure, we conducted a second test using a 350-km-diameter synthetic plume with −2% Gaussian velocity distribution centred at the highest amplitude points in the plume structure that we imaged using real data (Supplementary Fig. 7a). In the same way as our initial resolution test, we added a random distribution of noise with a standard deviation of 0.5 s to the synthetic data and used the same inversion parameters. The results (Supplementary Fig. 7b) show we were able to resolve the position and amplitude of the tilted structure in the lower mantle with similar success to our previous test, recovering the greatest amount of structure between 1,500 and 2,000 km in depth. However, the test does expose the inability of core waves to constrain subhorizonal features

in the upper portion of the mantle. Between 900 and 1,300 km depth, the increase in the plume's tilt and the near-vertical orientation of the SKS and SKKS ray paths prevents us from accurately resolving the structure there and as a result we see a notable drop in the recovered amplitude. A comparison between results using different starting models (Supplementary Fig. 5) show much larger variation in that depth range than at greater depths. Given the anomalies above and below that depth range and the low-amplitude anomaly we do detect, it is likely that the plume is continuous but strongly tilted, such that we are unable to fully resolve it there.

As a final check to determine the degree of vertical smearing in our experiment, we repeated the test above but added 500 km gaps to the plume (Supplementary Fig. 8a). The inverted model (Supplementary Fig. 8b) does show some vertical smearing in the lowermost mantle, but the artefact structures are much lower amplitude (~0.5%) than the real structure (>1%) and do not resemble what we imaged. Therefore, it is unlikely that the plume we identified is isolated slow anomalies being smeared together, but rather a continuous feature across the lower mantle.

Code availability. We are unable to make the computer code associated with this paper available. The finite frequency code we used was written by S.-H. Hung (National Taiwan University). The adaptive stacking code was written by S. Yu and E. Garnero (both at Arizona State University). The figures were made using GMT which can be downloaded here: http://gmt.soest.hawaii.edu/.

Data availability. For non-Canadian stations, we downloaded the waveforms from IRIS DMC using SOD (Standing Order for Data), which can be found here: http://www.seis.sc.edu/sod/. We downloaded for Canadian stations from the Canadian National Data Center via email request: http://www.earthquakescanada.nrcan.gc.ca/stndon/CNDC/index-en.php. The tomography model US-SL-2014[28] can be accessed here: http://ds.iris.edu/ds/products/emc-earthmodels/. S40RTS[25], SEMUCB-WM1[26], and TX2016[27] can be requested by contacting the corresponding author in each respective paper.

References

39. Rawlinson, N. & Kennett, B. L. N. Rapid estimation of relative and absolute delay times across a network by adaptive stacking. *Geophys. J. Int.* **157**, 332–340 (2004).
40. Dziewonski, A. M. & Anderson, D. L. Preliminary reference Earth model. *Phys. Earth Planet. Inter.* **25**, 297–356 (1981).
41. Thorne, M. S., & Garnero, E. J. Inferences on ultralow-velocity zone structure from a global analysis of SPdKS waves. *J. Geophys. Res. Solid Earth* **109**, B0301 (2004).
42. Muller, G. The reflectivity method: a tutorial.*J. Geophys. Zeit. Geophys.* **58**, 153–174 (1985).
43. Nolet, G. Imaging the Interior (Cambridge Univ. Press, Cambridge, 2008)..
44. Laske, G., Masters, G., Ma, Z. & Pasyanos, M. Update on CRUST1. 0 — A 1-degree global model of Earth's crust. In *EGU General Assembley* EGU2013–2658 (European Geosciences Union, 2013)..
45. Kennett, B. L. N. *Seismological Tables: ak135* 1–289 (Research School of Earth Sciences, Australian National University, Canberra, 2005).
46. Stein, S. & Wysession, M. *An Introduction to Seismology, Earthquakes, and Earth Structure* (John Wiley & Sons, 2009).
47. Liu, K. H. et al. A uniform database of teleseismic shear wave splitting measurements for the western and central United States. *Geochem. Geophys. Geosyst.* **15**, 2075–2085 (2014).
48. Currie, C. A., Cassidy, J. F., Hyndman, R. D. & Bostock, M. G. Shear wave anisotropy beneath the Cascadia subduction zone and western North American craton. *Geophys. J. Int.* **157**, 341–353 (2004).
49. Evans, M. S., Kendall, J. M. & Willemann, R. J. Automated SKS splitting and upper-mantle anisotropy beneath Canadian seismic stations. *Geophys. J. Int.* **165**, 931–942 (2006).
50. Frederiksen, A. W. Lithospheric variations across the Superior Province, Ontario, Canada: evidencefrom tomography and shear wave splitting. *J. Geophys. Res. Solid Earth* **112**, B004861 (2007).
51. Balfour, N. J., Cassidy, J. F. & Dosso, S. E. Crustal anisotropy in the forearc of the northern Cascadia subduction zone, British Columbia. *Geophys. J. Int.* **188**, 165–176 (2012).
52. Lee, D. K. & Grand, S. P. Upper mantle shear structure beneath the Colorado Rocky Mountains. *J. Geophys. Res. Solid Earth* **101**, 22233–22244 (1996).
53. Coleman, T. F. & Li, Y. An interior trust region approach for nonlinear minimization subject to bounds. *SIAM J. Optim.* **6**, 418–445 (1996).
54. Hansen, P. C. Analysis of discrete ill-posed problems by means of the L-curve. *SIAM Rev.* **34**, 561–580 (1992).